Remote Sensing of Environment 184 (2016) 139–152

Contents lists available at ScienceDirect

Remote Sensing of Environment

journal homepage: www.elsevier.com/locate/rse

The Airborne Snow Observatory: Fusion of scanning lidar, imaging spectrometer, and physically-based modeling for mapping snow water equivalent and snow albedo

Thomas H. Painter [a,*], Daniel F. Berisford [a], Joseph W. Boardman [b], Kathryn J. Bormann [a], Jeffrey S. Deems [c,d], Frank Gehrke [e], Andrew Hedrick [f], Michael Joyce [a], Ross Laidlaw [a], Danny Marks [f], Chris Mattmann [a], Bruce McGurk [g], Paul Ramirez [a], Megan Richardson [a], S. McKenzie Skiles [a], Felix C. Seidel [a], Adam Winstral [f]

[a] Jet Propulsion Laboratory, California Institute of Technology, Pasadena, CA, USA
[b] Analytical Imaging and Geophysics LLC, Boulder, CO, USA
[c] Cooperative Institute for Research in the Environmental Sciences, University of Colorado, Boulder, CO, USA
[d] National Snow and Ice Data Center, Boulder, CO, USA
[e] California Department of Water Resources, Sacramento, CA, USA
[f] USDA ARS Northwest Watershed Research Center, Boise, ID, USA
[g] McGurk Hydrologic, Orinda, CA, USA

ARTICLE INFO

Article history:
Received 7 October 2015
Received in revised form 16 June 2016
Accepted 24 June 2016
Available online 30 June 2016

Keywords:
Snow water equivalent
Snow albedo
Water resources
Scanning lidar
Imaging spectrometer

ABSTRACT

Snow cover and its melt dominate regional climate and water resources in many of the world's mountainous regions. Snowmelt timing and magnitude in mountains are controlled predominantly by absorption of solar radiation and the distribution of snow water equivalent (SWE), and yet both of these are very poorly known even in the best-instrumented mountain regions of the globe. Here we describe and present results from the Airborne Snow Observatory (ASO), a coupled imaging spectrometer and scanning lidar, combined with distributed snow modeling, developed for the measurement of snow spectral albedo/broadband albedo and snow depth/SWE. Snow density is simulated over the domain to convert snow depth to SWE. The result presented in this paper is the first operational application of remotely sensed snow albedo and depth/SWE to quantify the volume of water stored in the seasonal snow cover. The weekly values of SWE volume provided by the ASO program represent a critical increase in the information available to hydrologic scientists and resource managers in mountain regions.

1. Introduction

Snow cover and its melt dominate sources in many of the world's mountainous regions, and in adjacent areas dependent on river flows originating from mountain basins. In the western United States, snowmelt runoff dominates the surface water hydrology, providing >75% of the total freshwater (Bales et al., 2006). However, the region faces significant water resource challenges due to the intersection of increasing demand from population growth and changes in runoff volume and timing due to climate change (Christensen et al., 2004; Christensen and Lettenmaier, 2007).

Observations indicate an ongoing reduction in the seasonal duration of mountain snowpacks (Hamlet et al., 2005; Mote et al., 2005; Hamlet et al., 2007; Clow, 2010), a trend likely to continue under unimpeded warming associated with climate change (Christensen and Lettenmaier, 2007; Deems et al., 2013b). Moreover, increasing temperatures in desert systems will increase dust loading to mountain snow cover (Munson et al., 2011), thus reducing the snow cover albedo and accelerating snowmelt runoff (Painter et al., 2007; Painter et al., 2010; Skiles et al., 2012).

The two most critical properties for understanding timing and magnitude of snowmelt runoff are the spatial distributions of snow albedo and snow water equivalent (SWE) (Blöschl, 1991; Kirnbauer et al., 1994). Despite the importance of these properties in controlling volume and timing of runoff, the mountain snowpack remains poorly quantified around the globe (Bales et al., 2006) (Barnett et al., 2005), leaving runoff and climate models poorly constrained and our physical understanding of mountain snowmelt driven systems incomplete.

In the western US, we have relatively sparse measurements of SWE, mostly at lower and middle elevations and only a few per basin

* Corresponding author.
E-mail address: thomas.painter@jpl.nasa.gov (T.H. Painter).

http://dx.doi.org/10.1016/j.rse.2016.06.018
0034-4257/

(Bales et al., 2006). These measurements are used as indices for runoff estimates but, as point indicators for a measure that varies widely across the landscape from zero to >5 m, they do not provide a direct estimate of the total water volume stored in the seasonal snow-covered mountain basins, nor are they sufficient to support physically-based hydrologic models. Moreover, with rising snow line elevations under climate change, these index sites will more frequently melt out earlier and thus lose their utility (Nolin and Daly, 2006). Albedo is even more drastically under sampled. Only six sites have ongoing, multi-year measurements of snow albedo in the western US (Bales et al., 2006; Painter et al., 2012).

Recognizing the void in knowledge of the mountain snowpack, we developed the Airborne Snow Observatory (ASO), a coupled scanning lidar system and imaging spectrometer, to quantify snow depth, SWE, and snow albedo, to offer unprecedented knowledge of snow properties and distribution for cryospheric science, and to provide spatially comprehensive, robust inputs to water management models and systems of the future. Our overarching objective was to generate comprehensive time-series maps of coincident SWE and albedo over large mountain basins. To do this, we combined approximately weekly repeat lidar and spectrometer over-flights with snow density fields simulated by an energy balance snow model and constrained by in situ measurements, to convert the lidar-derived snow depths to distributed retrieval of SWE. ASO weekly over-flights were initiated in mid-winter, prior to peak SWE, and continuing throughout the melt season. These data provide a reliable estimate of total snow accumulation and ablation, and its spatial distribution during the snow season.

The ASO data set represents the first quantitative estimate of the dynamics of the volume and distribution, both spatial and temporal, of the seasonal snow cover in a mountain watershed. The ASO program is not only changing how science views mountain snowpack and hydrology, but is defining a new paradigm for water management that can be applied in snow-fed regions around the world. Here we describe the ASO in terms of its legacy from other systems, physical motivation for and description of instrumentation, algorithms, data processing, and a case study of the ASO in operation in the Tuolumne River Basin, California.

2. Background

2.1. Snow albedo

Albedo is defined as the percent of incident solar flux that is reflected by a surface. Albedo can be either *broadband* (integrated across wavelengths) or *spectral* (integrated over multiple narrow wavelength ranges) (Schaepman-Strub et al., 2006). With an imaging spectrometer, radiances in discrete bands across the complete spectrum (usually either 350–1050 nm (VNIR) or 350–2500 nm (VSWIR)) are sampled and then, through atmospheric correction and topographic correction, both the spectral hemispherical-directional reflectance factor (HDRF) and spectral albedo are retrieved (Green et al., 1998; Painter et al., 2013).

While imaging spectroscopy has long been used for retrieving snow properties (Painter et al., 1998; Nolin and Dozier, 2000; Painter et al., 2001; Painter et al., 2003; Painter and Dozier, 2004a; Green et al., 2006; Dozier et al., 2009; Painter et al., 2013), these papers have described what are very few acquisitions and have instead been primarily descriptions of technology/algorithm development and demonstration. Never have we had a time series of imaging spectrometer retrievals of albedo sufficient to constrain snowmelt models or to provide a quantitative understanding of the temporal variation of the spatial distribution of snow albedo. Mountain snowmelt is dominated by net shortwave radiation, itself controlled by snow albedo (Marks and Dozier, 1992; Oerlemans, 2000; Painter et al., 2015). Subsequently this lack of quantitative, spatially explicit and multi temporal albedo data to inform and constrain models has hampered efforts to reduce uncertainty in snowmelt simulations or to make models resilient to changing climate or snow impurity conditions (Blöschl, 1991; Kirnbauer et al., 1994; Painter et al., 2010; Bryant et al., 2013; Deems et al., 2013b; Sproles et al., 2013).

Imaging spectrometer retrievals give more accurate albedo determinations than do multispectral retrievals because of their comprehensive sampling of the radiance spectrum, such as the <1% broadband albedo uncertainties described in Painter et al. (2013). The standard snow albedo product distributed by the National Snow and Ice Data Center Distributed Active Archive Center (NSIDC DAAC) is embedded in the MOD10A1/MYD10A1 product suite. While on the Greenland Ice Sheet, the albedo product has uncertainties of 7–8% (Stroeve et al., 2005), in Arctic tundra regions the uncertainties of ~5% (Wang et al., 2012), and in mountain settings uncertainties of 5–15% (Sorman et al., 2007), all of these well outside of the 2% albedo requirement discussed below.

2.2. Snow water equivalent

Retrieving SWE from remote sensing has long been considered the so-called "Holy Grail" of snow hydrology (Dozier, 2011). Nearly every part of the electromagnetic spectrum has been explored for SWE retrievals – microwave (passive and active), gamma, and even optical in the case of thin snow (Dozier et al., 1981) – and yet reliable success has been largely elusive.

Given the sensitivity of microwave radiation to SWE in ideal settings, much effort has been put toward passive microwave and radar techniques. For several decades, SWE has been retrieved from passive microwave sensors (e.g. the Special Sensor Microwave Radiometer (SSMR), SSM/I, AMSR-E) but with great uncertainties and only on relatively homogenous and low-slope terrain with SWE < ~150 mm (Chang et al., 1996; Luojus et al., 2013). For a snowpack with a density of 300 kg m^{-3}, this 150 mm saturation equates to a snow depth of 0.45 m, which represents a very shallow depth for mountain snowpacks, where depths can reach to >10 m. GlobSNOW, considered the best current retrieval algorithm for SWE globally, only infers retrieves SWE for regions outside of mountains (standard deviation of topography within an EASE-Grid cell must be <200 m) due to the complexity of the signal with myriad terrain facets soil moisture, ground ice and standing water, or liquid water or ice lenses in the snowpack (Takala et al., 2011; Luojus et al., 2013).

Radar retrievals have shown potential for direct and inferred retrievals of SWE (Shi and Dozier, 2000b; Shi and Dozier, 2000a; Yueh et al., 2009). For mountain snow cover, radar retrievals have particular sensitivities to grain size stratigraphy, liquid water in the snowpack absorbing the radar signal, and terrain layover. Moreover, considerable mid-latitude snow lies below timberline and, as such, multiple scattering by trees and the absorption of the radar signal by canopy water occludes retrievals in this critical elevation range. Perhaps the most important period for assimilation of SWE information for hydrologic modeling is when the snowpack is wet. Therefore, the combination of loss of signal due to snow wetness and vegetation canopy, along with layover in complex terrain, makes radar suboptimal for remote sensing of mountain SWE.

Snow water equivalent is mapped operationally by the National Weather Service National Operational Hydrologic Remote Sensing Center (NOHRSC) with a data assimilation model leveraging multiple data sources including airborne passive gamma radiation surveys (Peck et al., 1980; http://www.nohrsc.noaa.gov/snowsurvey/). Terrestrial gamma emission from radioisotopes in the soil column is attenuated by water of any phase. Gamma retrievals conducted prior to snow accumulation in the fall provide a background emission value at pre-snow soil moisture levels, and again during the snow-covered season, the difference used to produce a single mean areal SWE estimate from the integral of the flight line (Carroll, 2001). This integrated estimate, while being spatially explicit along a flight line and for a particular drainage, is challenged by complex terrain and vegetation cover, and lacks the spatial extent and detail to determine a true basin-wide spatial

distribution. Furthermore, the Gamma SWE signal can be confounded by changes in soil or vegetation water content that occur after the snow-free flight. However, the NOHRSC program is targeted at the continental scale, incorporating the gamma SWE retrievals along with an array of satellite SCA and in situ snow and meteorological observations into a model assimilation scheme to estimate SWE and snow cover properties (SNODAS). This operational service provides a benchmark upon which finer-scale snow mapping efforts such as ASO can build by adding basin- to slope-scale snow cover information within the broader context. This higher resolution information could be incorporated into a modeling system such as NOHRSC SNODAS via assimilation.

Recent studies have demonstrated the suitability and accuracy of airborne and terrestrial lidar data for differential (or geodetic) mapping of snow depth in mountainous terrain (Hopkinson et al., 2004; Deems et al., 2006; Trujillo et al., 2007; Prokop, 2008; Mott et al., 2011; Deems et al., 2013a; Deems et al., 2015). The lidar system measures range-to-target for each emitted laser pulse, with each target location geolocated when combined with platform positioning and attitude data, creating a point cloud of elevation measurements. Differencing snow-free from snow-covered surface elevation data sets allows a straightforward, robust calculation of snow depth. Snow depth variations comprise the majority of the spatial variation in SWE, as snow density variation is more conservative (Fig. 1) (Sturm et al., 2010). Snow depth measurements can then be combined with simulations of snow density distributions to obtain SWE values for the full lidar data extent, much like the estimates of ice sheet mass fluxes from ICESat-1 and other altimetry missions (Bamber and Rivera, 2007). By differencing two direct elevation measurements we avoid the issues of snow wetness, snow layer and grain size stratigraphy, canopy occlusion, layover, and surface roughness that complicate retrieval of SWE from other remote sensing techniques.

3. System description

The Airborne Snow Observatory draws on a heritage of precursor airborne imaging spectrometer/scanning lidar systems developed for next generation ecosystem science and mapping. The current AToMS configuration of the Carnegie Airborne Observatory, as well as its predecessor systems, have made breakthrough discoveries in tropical forest ecology using this integrated concept (Asner et al., 2012; Asner et al., 2013). Similarly, the National Ecological Observatory Network is actively developing and deploying a triplet of similar systems for their Airborne Observation Platforms, an integral element of their multi-discipline, multi-decade, continental-scale ecological measurement campaign (Kampe et al., 2010).

The Airborne Snow Observatory is the first such system designed specifically for snow and water resources monitoring and research. The time-critical nature of the snow data coupled with the relatively large and complicated mountain areas that need to be measured, drive the system to high altitude flight, wide swaths, and optimized processing. The resulting ASO system is unique in two aspects: (a) the joint inversion of the active lidar and passive imaging spectrometer data coupled to an energy balance snow model for full SWE and snow albedo retrievals and (b) the sub-24-hour latency for full product generation and delivery.

3.1. Imaging spectrometer

ASO uses an *itres* CASI 1500 imaging spectrometer to retrieve spectral albedo and spectrally-integrated albedo across the majority of the significant solar irradiance at Earth's surface. These retrievals allow discrimination of the impacts on albedos of changes in snow surface grain size and radiative forcing by dust, black carbon, and organic material. ASO's spectrometer measures reflected radiance at ~10 nm spectral resolution across the wavelength range 380–1050 nm. The CASI 1500 has an instantaneous field of view (IFOV) of 0.49 mrad and an angular uncertainty of 0.0024 mrad (*itres* Research Limited, www.itres.com). The dynamic range is covered with 14-bit and signal to noise ratio of 300–600 across the visible wavelengths, and 500 in the near-infrared down to 100 near 1050 nm. The instrument field of view is ±20° (Fig. 2) and ASO uses integration times of 12–14 ms over snow to balance reduction of saturation on steep illuminated peaks and deep shadowed valleys.

3.2. Scanning lidar

ASO uses a Riegl Q1560 airborne laser scanner (ALS) to measure surface elevations from which we calculate snow depths. The Q1560 uses dual 1064 nm wavelength lasers, each with a 60° scan angle (±30° across nadir), and with a 14° angle relative to the cross-track axis, producing an up to 8° fore/aft look angle (off-nadir in the along track direction) (Fig. 2). We use a 1064 nm wavelength system because of its

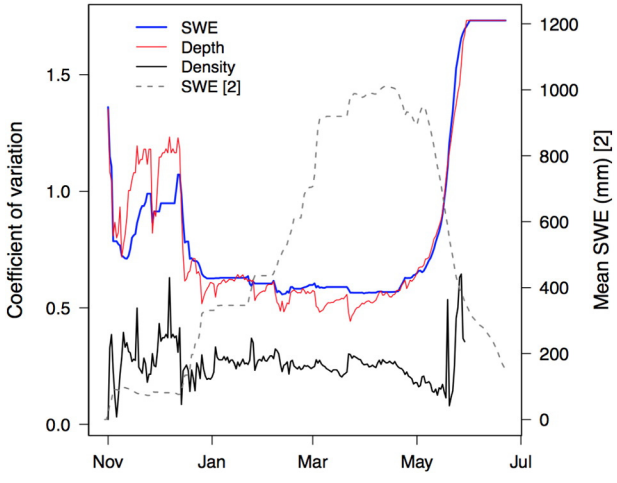

Fig. 1. Typical seasonal time series of the coefficient of variation of SWE, depth, and density, demonstrating that the greatest variation in SWE comes from the variation in depth. The coefficients of variation are calculated regionally using daily SWE and depth data from eight SNOTEL sites throughout the eastern Sierra Nevada in California. The data shown is from the 2009 water year, however all years from 2003 to 2010 show a similar pattern.

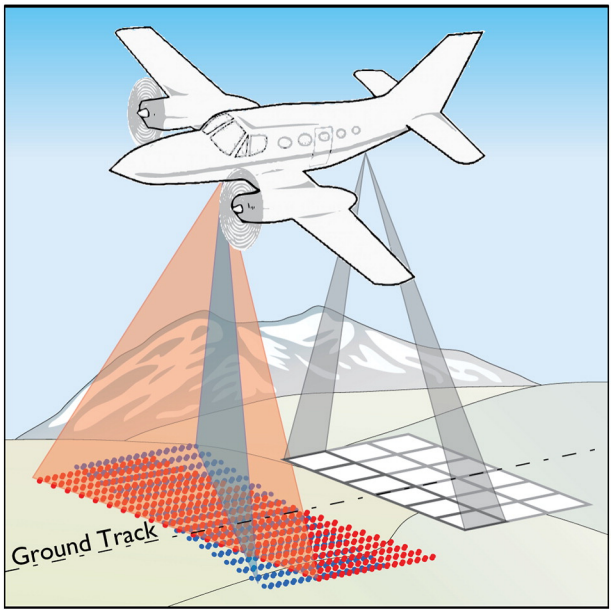

Fig. 2. Scan configuration of ASO scanning lidar (Riegl Q1560) in color and imaging spectrometer (Itres CASI-1500) in grayscale.

relatively small laser penetration depth in snow and relatively high snow reflectance at that wavelength, as well as greater penetration through vegetation canopies (Deems et al., 2013a).

The scan system parameters provide an effective field of view of 58°. The laser pulse repetition rate (PRR) ranges from 100 to 800 kHz with an effective measurement rate of up to 532 kHz with the 60° scan angle. The laser beam divergence is ≤0.25 mrad, which at nadir and 5000 m range is ≤ 1.25 m. The angle measurement resolution is 0.001°. The nominal maximum range according to manufacturer for surfaces with reflectance ≥ 60%, such as that of fine-grained snow, is 5800 m for PRR of 200 kHz. However, ASO test flights have found strong consistent returns from >8000 m (not presented here). The scanning lidar has a pointing uncertainty of 0.001°. With the inertial measurement unit (IMU) aircraft attitude uncertainty of 0.011°, the functional angular uncertainty of the aircraft-lidar system is 0.012°.

The high PRR can result in emission of a laser pulse prior to detection of a return signal from the prior pulse, known as "Multiple Time-Around" (MTA), resulting in range ambiguity. The maximum unambiguous range R_u is a function of the PRR and the speed of light c:

$$R_u = \frac{c \cdot PRR^{-1}}{2} (\mathrm{m}) \quad (1)$$

and multiples of R_u are termed MTA zones. The Q1560 uses a novel method to resolve range ambiguities, whereby a high frequency, random time "jitter" is applied to the PRR, and when consecutive returns from a single scan line are compared, the standard deviation of elevations is minimized when the returns are assigned to the proper MTA zone (Rieger and Ullrich, 2011). This automated procedure allows the use of high PRR at flight altitudes (AGL) much greater than R_u, and produces high ground point densities from high altitudes where the scan swath is wide, optimizing survey efficiency.

3.3. Inertial measurement unit

Accurate ray tracing and the resulting data co-registration and alignment of the lidar and imaging spectrometer data are fundamentally critical in the ASO system, its processing software, and its science objectives. The required level of geolocation accuracy is achieved through the use of a single lidar-integrated Trimble Applanix POS/AV 510 GPS and Inertial Measurement Unit (IMU). The IMU has angular uncertainties of 0.005°, 0.005° and 0.008° in roll, pitch, and true heading after post processing, and a resultant attitude uncertainty of 0.011°. The GPS/IMU is mounted internally in the scanning lidar, simplifying lever arm measurement and boresighting. Postprocessing of the raw position and attitude data stream includes differential correction of the GPS positions using ground GPS base station data or broadcast corrections from the Trimble RTX service (http://www.trimble.com/positioning-services/centerpoint-RTX.aspx), resulting in a Smoothed Best Estimate of Trajectory (SBET) file.

4. Fusion of spectrometer and lidar data

The accurate geolocation of both the lidar and imaging spectrometer data sets is critical to achieving the registration necessary for the successful joint inversion of the two data sets in the processing phase. The lidar and spectrometer are mounted to a rigid Payload Integration Mount (PIM), and thus the lever arm offsets between the spectrometer and the lidar-integrated GPS/IMU are easily modeled and maintained. The PIM provides a single rigid platform that defines the body frame of the navigation solution, mounted over the nadir-looking port of the ASO aircraft. With the rigid PIM and the accurate GPS/IMU we have the time sync, position, and attitude information needed to geolocate and register the two data streams, forming the basis of the critical data integration and fusion.

We process the GPS/IMU and lidar data according to the manufacturer's protocol, using available base station records or Trimble CenterPoint RTX real-time broadcast for differential position correction. Once the lidar data are georeferenced, the derived digital surface model (DSM) is combined with the position/attitude data (SBET file) to orthorectify the imaging spectrometer data (Fig. 3), leveraging the coincident and highest-resolution surface model for imaging spectrometer ray tracing and rendering. The separately recorded imaging spectrometer data are linked to the SBET data set via time stamps on each spectrometer image cube frame, adjusted for any time biases derived from in-flight calibration experiments.

We perform camera calibration and time synchronization experiments in flight to fully characterize the look directions of each imaging spectrometer pixel allowing us to correct time bias, if any, between the lidar and imaging spectrometer data streams. Using a nonlinear inversion that is fed with control points picked from matching lidar intensity and spectrometer image features, we solve for the three direction cosines of each imaging spectrometer cross track pixel. The retrieved accuracy is typically sub-pixel. Using sharp aircraft roll excursions to distort a linear ground feature, we solve for the time bias achieving precision approaching a microsecond.

Fig. 3A shows the before and after imagery for a successful test for time synchronization. Fig. 3B shows matched imagery subsets of lidar intensity and imaging spectrometer radiance, after camera modeling, to achieve sub-pixel co-alignment. The critical ASO fusion of the disparate data types rests sequentially on the accuracy and precision of the GPS/IMU data, the processed lidar returns, the rigidity of the payload integration mount, and finally the stability of the imaging spectrometer time bias and camera calibration. ASO end-to-end performance shows

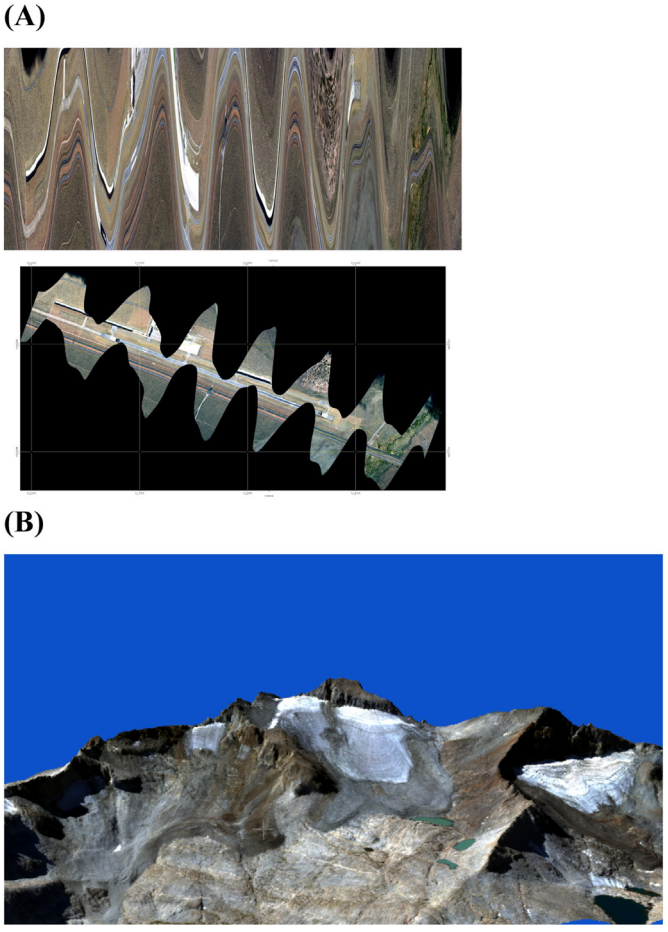

Fig. 3. Orthorectification of ASO data. (A) timing calibration through wiggle testing over an airport runway. (B) Alignment of spectrometer data with topography.

that all links in this mission-critical chain are maintaining stability and uniformity.

5. Science and operation implementation

Given the rapidly changing nature of snow cover presence, depth, and surface properties that modulate its melt, ASO flies target basins on a weekly basis from midwinter through complete snowmelt. The primary data product from the ASO imaging spectrometer is *snow albedo* and from the ASO lidar is *snow depth*, which we combine with modeled snow density to infer *SWE*. Supplementary products include fractional snow covered area, snow surface grain size, dust/black carbon radiative forcing, and land surface classification.

5.1. Flight operations

In the flight planning process, constant altitude flight lines are drawn to provide 15–20% overlap for the 40° FOV spectrometer over the highest terrain (the region with the least overlap) within the swath of each line (Fig. 4). Whenever possible, the direction of flight lines are planned to optimize flying in or near the solar principal plane to avoid snow forward scattering peaks (Painter and Dozier, 2004a; Painter and Dozier, 2004b).

5.2. Scanning lidar workflow and products

The scanning lidar data are converted from raw data to georeferenced point clouds, then to raster and finally used in the calculation of snow depth. Through assimilation of distributed snow density information, the snow depth data are then converted to SWE.

5.2.1. Elevation point clouds and gridded products

Processing from raw flight data to geolocated point cloud is handled by vendor-specific software (Riegl RiPROCESS). The return energy waveforms recorded by the sensor are converted to discrete returns via a Gaussian deconvolution algorithm (Riegl RiANALYZE; Wagner et al., 2006). In this processing step, which is accomplished in parallel using GPU processing, returns are also assigned to the proper MTA zone (Rieger and Ullrich, 2011), a into a scanner-oriented coordinate system, corrections for atmospheric conditions are applied, and an initial classification into vegetation/non-vegetation is conducted using a decision tree split on target number and pulse width. The resulting point cloud is then converted into a global coordinate system by applying a transformation that includes the corrected trajectory and platform orientation information from the integrated GPS/IMU (Riegl RiWORLD). Next, a manual geometric transformation converts the return records from the range/scan angle domain examination of overlapping data from adjacent and crossing flight lines is performed to ensure no systematic offsets or errors are present – none have been encountered to-date, however any between-line offsets would be corrected using the Scandata Adjustment tool in RiPROCESS, a plane- and point-matching algorithm used for boresight calibration. The final point cloud is written to LAS-format binary files for use in further postprocessing steps.

Several intermediate lidar products are next generated from the point elevation data, which allow characterization of the data set and survey parameters (Fig. 5). Point density, number of returns per pulse, and return intensity grids are all used for qualitative data consistency checks.

To identify ground points in forested areas, points tagged as "last return" are classified using the Multiscale Curvature Classification (MCC) algorithm (Evans and Hudak, 2007). The MCC algorithm applies successive curvature interpolation thresholds to iteratively classify points

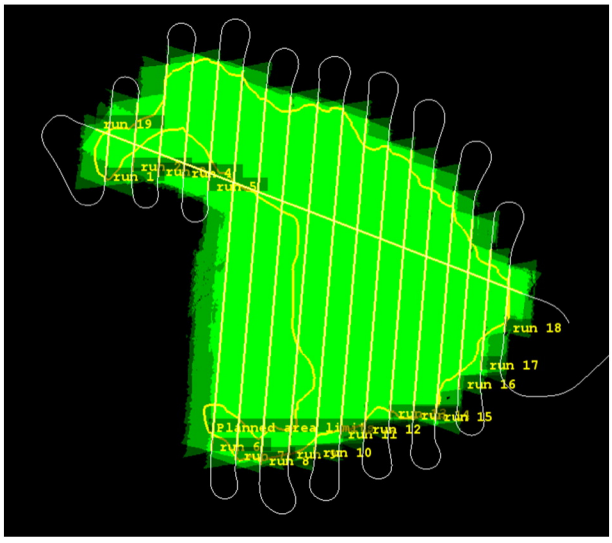

Fig. 4. Example ASO acquisition footprints over the Merced Basin, CA for May 3, 2015. Actual flight lines trajectories with lidar overlap expressed in transparent green. (For interpretation of the references to color in this figure legend, the reader is referred to the web version of this article.)

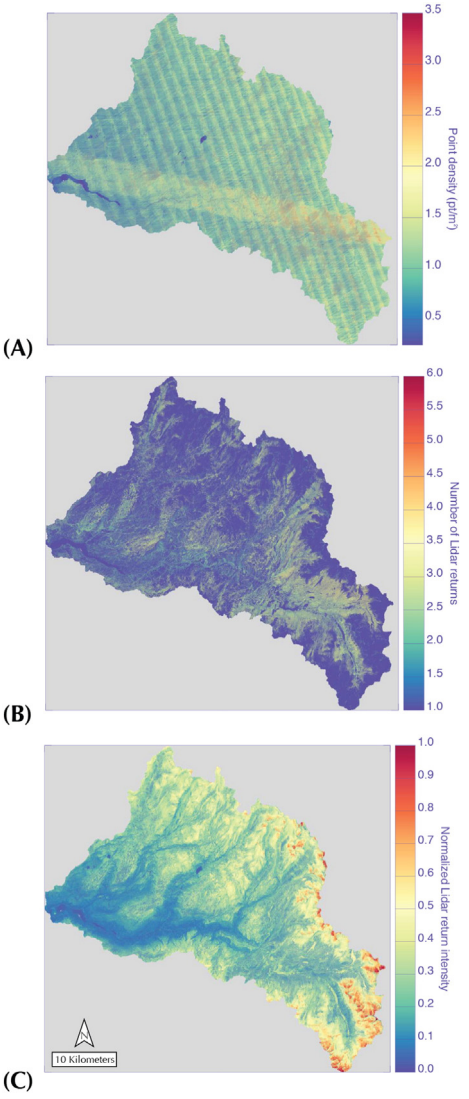

Fig. 5. ASO lidar acquisitions in distillation to raster for Tuolumne River Basin, CA for April 7, 2014. (A) Point density. (B) Number of returns per pulse. (C) Backscatter return intensity.

above each spline-interpolated surface as "not ground". The remaining points, classified as "ground", are then interpolated to a DTM representing the snow-free or snow-covered surface in the forested areas (Fig. 6).

In parallel, a DSM is produced from the mean of all first returns in each cell; this elevation grid, representing the solar-reflecting surface is used for ray-tracing in the spectrometer processing chain (see Section 5.3.1). The two separate gridded surfaces produced from first returns and from the MCC-classified point cloud elevation measurements, respectively, are then subjected to a void-filling routine – any data voids within the basin are filled starting with a 3×3 search window and increasing on odd integers (5,7,9,11,13) up to 15×15 pixel search window from which the mean elevation in the relevant window is used to fill voids (Fig. 6). Any remaining voids along with the broader areas outside the basin boundary are backfilled using the National Elevation Dataset (NED) for snow-free conditions and the most recent ASO DSM for snow-on conditions. NED data are adjusted vertically to convert from geoidal/orthometric to ellipsoidal as the ASO standard. The resulting void-filled and backfilled snow-off DTMs are then used as the reference for differencing from the snow-on DTMs to produce gridded snow depths.

5.2.2. Snow depth

Snow depth maps are a core component of the ASO processing (Fig. 7, Table 1). Our operational efforts to date use the straightforward approach of subtracting snow-off gridded surfaces from snow-on gridded surfaces. Our survey domains are characterized by areas of forest cover as well as extremely rugged topography, which complicate snow depth retrieval via simple surface subtraction. Even small errors or variations in locations can give erroneous snow depth in locations like the Sierra Nevada with steep, nearly vertical terrain and tall narrow trees.

To minimize the impacts of terrain- and forest-induced errors, we create two separate sets of snow-on and snow-off gridded surfaces from first returns only (i.e. no above-ground returns) and from MCC-classified ground points, as described above. From these, we build two gridded snow depth sets. We then employ a suite of masks using the spectrometer data and the lidar return-per-pulse grids to define complementary areas dominated by single returns (devoid of trees and vegetation) and areas with vegetation spectral signatures and multiple discrete returns per lidar pulse (where trees are present). A final composite snow depth grid is generated from merging the single return

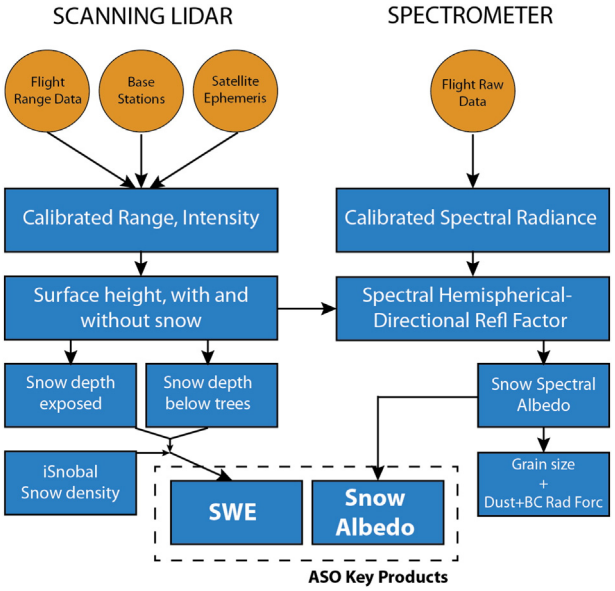

Fig. 7. The ASO LIDAR and spectrometer (CASI) pipelines, shown on the left and right, respectively.

differences (bare areas) and the MCC differences (treed areas) based on these masks.

Short vegetation such as grasses and shrubs tend not to have multiple lidar returns due to beam divergence from the altitudes at which ASO flies. Therefore, the ground return is largely unambiguous and as such, the overburden of snow in winter/spring results in generally robust retrievals of snow depth. However, shrubs can create cavities in the snow column and as such create a snow depth scenario that the lidar cannot detect. Further work investigating the impact of such scenarios and how geographically relevant they are would be helpful.

5.2.3. Snow water equivalent

From snow depth, we then can calculate SWE through a pixel-wise product of the ASO determined snow depth, z (m), and a spatially-distributed snow density, ρ_{snow} (kg m^{-3}), estimated using a snowpack evolution model and in-situ data (Fig. 8). SWE is often expressed in

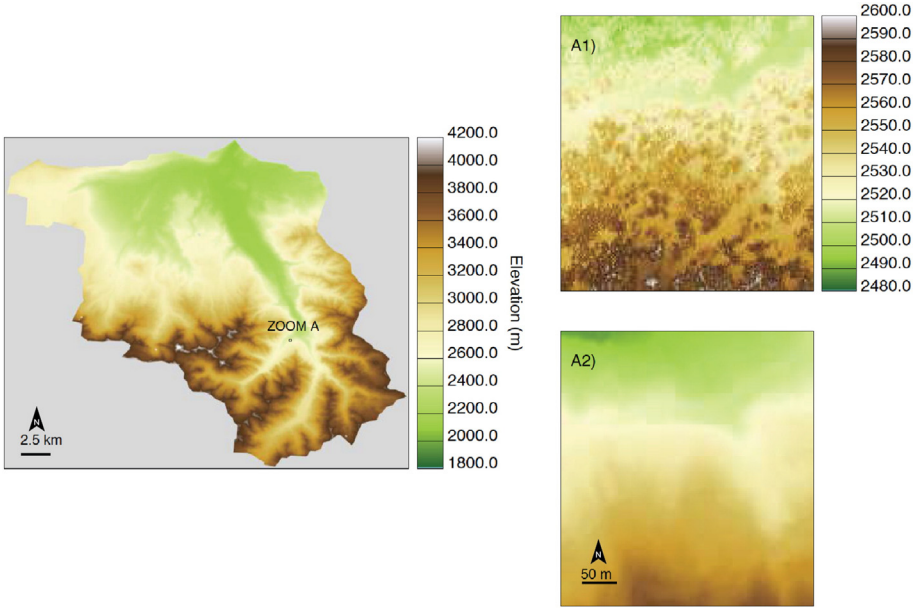

Fig. 6. Topographic data from ASO for Uncompahgre Basin, CO. (Left) Basin digital surface model. (A1) Zoom window of DSM. (A2) Zoom window of digital terrain model (bare earth).

Table 1
Core product suite of the Airborne Snow Observatory.

ASO product type	Spatial representation
Snow depth	Raster: 1.5, 3.0, 50.0 m
Snow water equivalent	Raster: 50 m Hydrologic response units Basin integrated Subbasin integrated Elevation bands
Snow albedo	Raster: 1.5, 3.0, 50.0 m Hydrologic response units
Grain size and radiative forcing by impurities	Raster: 1.5, 3.0, 50.0 m

either of two units: kg m^{-2} or m. The former gives the mass of water per unit area and is determined by:

$$SWE = z \cdot \rho_{snow}\left(\text{kg m}^{-2}\right) \quad (2)$$

The latter is determined by dividing the former by the density of water (1000 kg m^{-3}) to provide SWE (m) as the depth of water if the snowpack is melted completely:

$$SWE = \frac{z \cdot \rho_{snow}}{\rho_{water}}(\text{m}) \quad (3)$$

5.2.3.1. Snow density modeling. Pixel-wise simulated snow densities that are available within 24 h of the lidar/spectrometer acquisitions are a key component of the snow depth to SWE conversion calculations in Eqs. (2) and (3). Although basin and regional-scale SWE distribution is largely controlled by snow depth variability (Jonas et al., 2009, Fig. 1), the spatial, seasonal and inter-annual dynamics of snow density can be non-trivial (Sturm and Holmgren, 1998; Bormann et al., 2013) and must be incorporated into the conversion to reduce uncertainty in the final SWE product.

We employ a raster-distributed physically-based energy-balance model, *iSnobal* (Marks, 1999), that explicitly simulates snow density to provide pixel-wise snow density estimates in near-real time throughout the season (Fig. 8B). Physics-based numerical snow models (e.g. SNTHERM (Jordan, 1991), SHAW (Flerchinger et al., 1994), UEB (Tarboton et al., 1995; Tarboten and Luce, 1996), and SNOWPACK (Bartelt and Lehning, 2002)) such as *iSnobal* are a logical choice for providing the distributed snow density estimates required to support the production of ASO SWE products as they a) capture important physical processes for snow density; b) may be incrementally advanced in near-real time at basin-scales through the length of the snowmelt season, and c) can be made available at fine spatial and temporal resolutions.

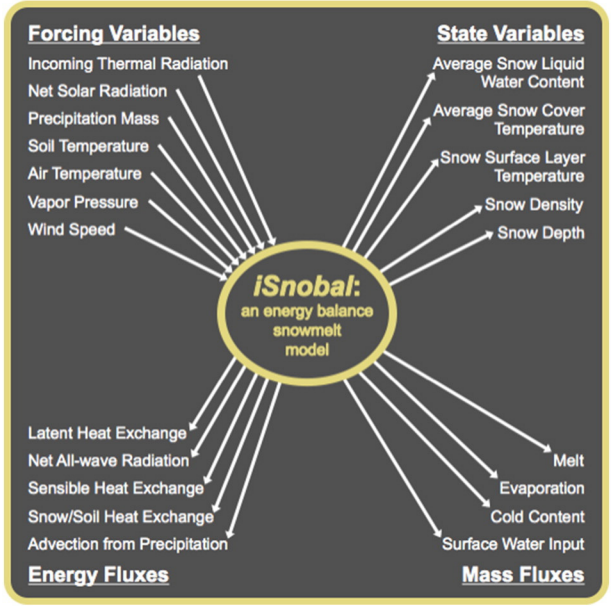

Fig. 8. USDA – ARS snow model *iSnobal* forcing data parameters, state variables, and energy and mass flux outputs.

In particular, *iSnobal* is ideal for this application as it is numerically efficient, representing the snowcover as a two-layer system, a thin active layer (10–25 cm) representing interaction of the snow cover with the atmosphere, and a variable-thickness secondary layer representing the rest of the snowcover. The model is forced with net solar rather than incoming solar radiation, in anticipation of being able to derive albedo from remote sensing data. Snow depth and density are state variables, making *iSnobal* ideal for integration with ASO products (see Figs. 8–9). It is noteworthy that *iSnobal* is one of the few energy balance snow models where snow density is a standard output. Though the model was developed >25 years ago, it was designed specifically for integration with remotely sensed data (Marks and Dozier, 1992), capable of updating and restarting as a new state condition is derived from remote sensing. ASO output products – spectral albedo and snow depth – are essentially the first remotely sensed products to be available for this purpose.

iSnobal calculates snow density using time-based algorithms that account for snow aging, mechanical compaction, the impact of liquid water with adjustments for new snow deposition. Previous applications of *iSnobal* have shown that the model is highly successful when measured and simulated SWE are compared across a wide range of scales and mountain environments (Link and Marks, 1999; Marks et al., 2002; Garen and Marks, 2005; Reba et al., 2011; Nayak et al., 2012; Kumar et al., 2013; Kormos et al., 2014; Rasouli et al., 2015). The ASO application is the first in which simulated snow density from *iSnobal* is the principal model output. Though the existing density algorithm is relatively simplistic, it produces reasonable results that are within 5–8% of measured values (see Fig. 15). However, we are working on improving the model density function to better represent the effects of snow depth, and expect to have an updated version within the next year.

Despite the very high spatial resolution of the lidar-derived snow depth data (3 m), the snow model is simulated at a coarser resolution (50 m) to reduce compute time and accommodate the quick data turnaround. The ASO snow depths are therefore first aggregated to 50 m resolution to match the snow model output prior to the conversion from depth to SWE. The limiting forcing data parameter for the iSnobal modeling is producing an estimate of precipitation distribution and phase. Integration of the ASO snow depth product into the iSnobal modeling data stream is planned for this year, and should largely eliminate this issue. Finally, modeled snow densities from iSnobal are adjusted to correct for elevation bias and then constrained by in-situ observations prior to the SWE calculation (Eq. 3), we discuss this process in more detail in Section 5.

5.3. Imaging spectrometer products

The main imaging spectrometer product for ASO is the snow albedo (Fig. 9). However, several intermediate and final products are also produced and delivered. Among these are spectral radiance, hemispherical-directional reflectance factor, spectral albedo, snow surface grain radius, and radiative forcing by light absorbing impurities.

5.3.1. Orthorectification

Orthorectification for science data is best understood as two distinct and wholly separate steps: ray tracing and rendering. Ray tracing involves developing and utilizing the parameters of the individual look direction of each datum to recover the x,y,z locations of its intersection with the ground surface. Rendering, by contrast, involves resampling or modeling the data to be presented or used in a regular grid despite

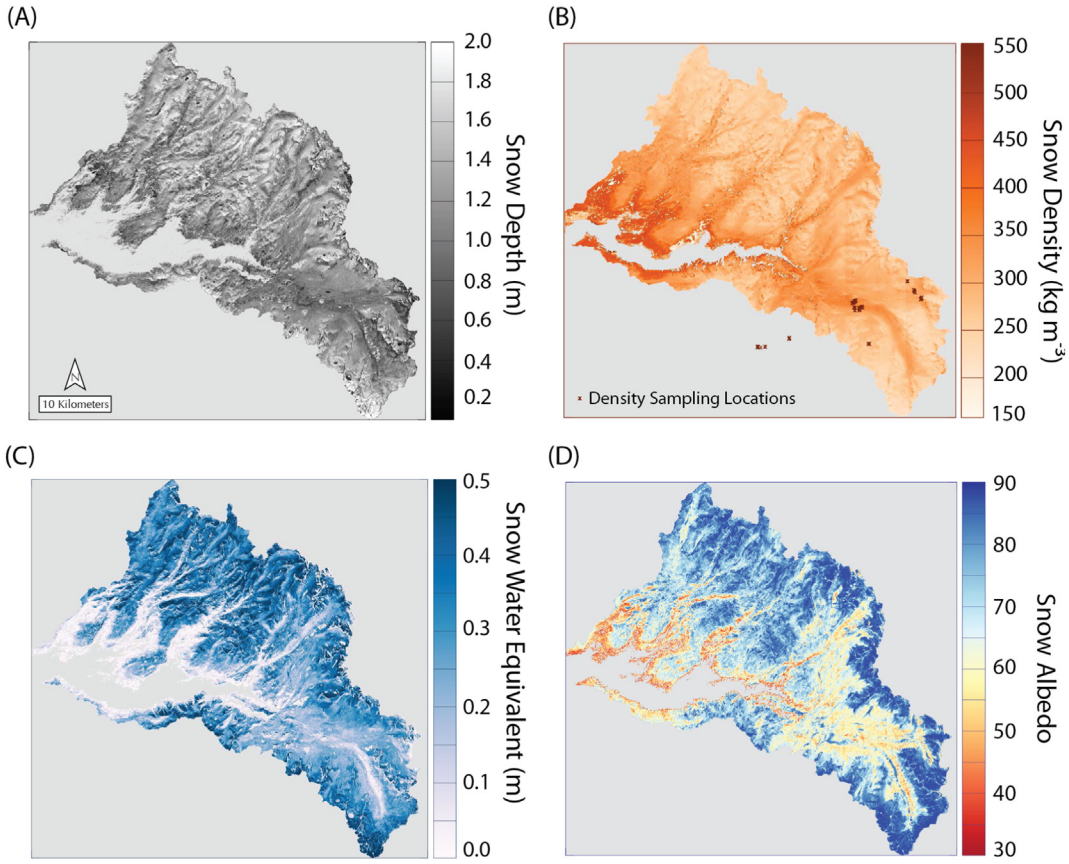

Fig. 9. ASO product suite for Tuolumne River Basin, April 7, 2014. (A) Snow depth map. (B) Snow density map with in-situ sampling locations (n = 180) The snow density observations were obtained during 2013 during four field campaigns spanning 5.5 weeks from 25th March to 3rd May. (C) Snow water equivalent. (D) Snow albedo.

the inherently irregular nature of the actual ground points acquired in flight. ASO uses ray tracing and rendering software specifically tailored to the unique nature of both the lidar and the imaging spectrometer images. For each data type, we create products using both the native format (non-rendered) and the gridded data sets, as required by the science processing data flow.

The first return gridded surface (Section 5.2.1) is used as a digital surface model onto which the imaging spectrometer data are ray traced. The imaging spectrometer data are ray traced pixel by pixel using the time/position/attitude data along with the calibrated camera model and time bias calibration. Each geolocated spectral sample is recorded in a binary file, as well as ten angular and distance metrics associated with the to-sun and to-sensor vectors for each observed spectrum. The rendered imaging spectrometer data are registered to the lidar DSM using a sample and line lookup table that specifies which spectrum from the non-rendered data cube occupies each DSM grid cell.

5.3.2. Spectral radiance

We calculate spectral radiance for the CASI 1500 data using the itres proprietary calibration software radcorr, giving 72 spectral bands from 380 to 1050 nm in units of $\mu W\ cm^{-2}\ sr^{-1}\ nm^{-1}$. This step is constrained by the most recent calibration file of the CASI 1500 spectrometer (Fig. 7).

5.3.3. Snow spectral and broadband albedo

We retrieve snow spectral and broadband albedo with the algorithm suite described in Painter et al. (2013) (Fig. 10). These algorithms use the local illumination and view geometries from the coincident DSM to determine the mapping of each radiance spectrum to its associated spectral albedo (Richter and Schläpfer, 2011), based on modeling of single scattering by ice particles from Mie theory (Mie, 1908) and multiple scattering from the discrete ordinates solution to the radiative transfer equation (Stamnes et al., 1988; Painter et al., 2003; Painter et al., 2013). The uncertainty in broadband albedo with the NASA Airborne Visible/Infrared Imaging Spectrometer (AVIRIS) is <0.5% (Painter et al., 2013). The uncertainties with the ASO spectrometer are assumed to be similar, but will be evaluated during field campaigns in spring 2016.

5.3.4. Snow surface grain size

Snow surface grain size is an important indicator of snow metamorphism and also provides a foundation from which to determine radiative forcing. With ASO, we use the grain radius retrieval described in Painter et al. (2013), which has grain diameter uncertainties of 20 to 50 μm across typical grain size range. This algorithm uses the ice absorption feature that has maximum absorption at 1030 nm. Uncertainties in these retrievals will also be further evaluated during ASO field campaigns in spring 2016.

5.3.5. Radiative forcing by light absorbing impurities

Radiative forcing by dust and carbonaceous particles is also retrieved during processing using the algorithm described in Painter et al. (2013). This model first determines the spectral albedo differences between the spectral albedo from ASO observations and the associated clean snow spectral albedo with the same grain radius, as determined above. In the reflectance calculation with ATCOR-4, direct, diffuse, and total spectral irradiances are calculated for clear-sky conditions under which ASO usually operates. We then band-wise multiply the spectral albedo difference by the calculated spectral irradiances and sum these for the instantaneous radiative forcing by dust and black carbon. The retrieval has a nominal uncertainty of $2.1 \pm 5.1\ W\ m^{-2}$ (Painter et al., 2013).

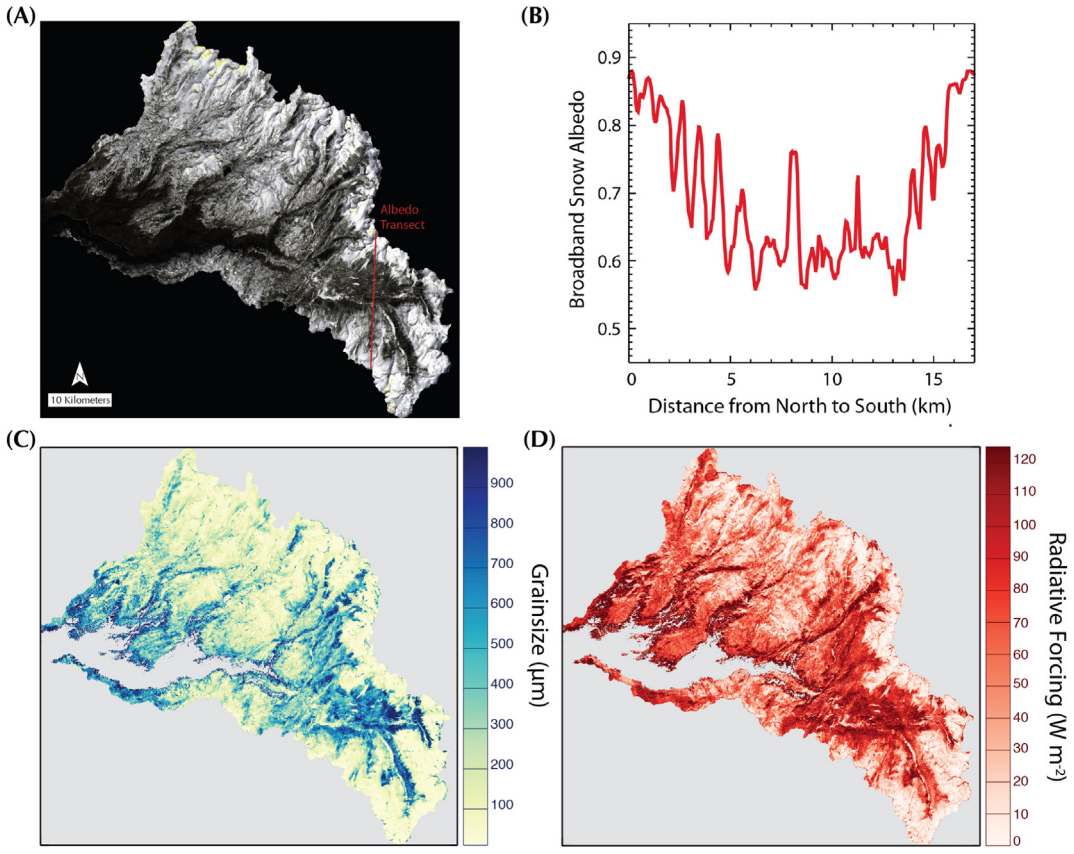

Fig. 10. Example ASO spectrometer products for Tuolumne River Basin, CA for April 7, 2014. (A) Natural color composite (R:652 nm, G: 557 nm, B: 461 nm) with transect indicated. (B) Broadband albedo along the transect indicated in (A). (C) Basin scale grainsize map. (D) Basin scale radiative forcing map.

5.4. Data system

Driven by the water management thread of the ASO program, data processing has a requirement of sub-24 hour latency for product turnaround and delivery. Because of the large data volumes produced, it is not possible to push the raw data via Internet to JPL in a timely fashion. Therefore, we are compelled to site the computing capacity at a location near the operations airport.

The ASO Mobile Compute System (MCS) is an end-to-end deployed data processing system replete with data systems software including: the Apache Object Oriented Data Technology (OODT) (Mattmann et al., 2006; Mattmann, 2009) data processing framework and the Apache Tika content detection and analysis toolkit (Mattmann and Zitting, 2011). Apache OODT provides file management, workflow and resource management, and an automated remote data acquisition system, automated file crawler, and science algorithm integration system. The Apache Tika toolkit allows automatic file identification, language detection and text/metadata extraction from any type of file.

6. Results

ASO was first fully deployed at the approximate time of peak SWE in early spring 2013 covering the Tuolumne River Basin in Yosemite National Park, California, a snowmelt-dominated basin above the O'Shaughnessy Dam on Hetch Hetchy Reservoir. This reservoir provides fresh water supply and hydropower for the City and County of San Francisco and other Bay Area municipalities. ASO has thus far acquired complete coverage of the Tuolumne River Basin beginning at roughly the time of peak SWE in early spring of 2013 and 2014, and beginning in mid-February of 2015 through meltout. Below we demonstrate results from 2014 – in that year, ASO acquired data 11 times over the Tuolumne Basin from 23 March to 5 June, covering the period from maximum snow accumulation until near complete melt out.

6.1. Retrievals

The core products, along with the snow density map, for the Tuolumne Basin on 7 April 2014 are shown in Fig. 9. The spatial maps of snow depth show complex spatial variability across the Tuolumne basin that is not simply correlated with elevation (Fig. 8A). The mean snowline elevation was approximately 2120 m for this acquisition with 69% of the basin covered in snow >0.1 m deep. As expected, shallow snow cover (<0.5 m) is observed at low elevations near the snowline, but shallow snow is also common along exposed ridgelines at high elevation (>3400 m). There is a prominent high accumulation zone in the southeast corner of the basin, with snow depths >2 m.

From the product of the snow depth and the snow density fields (Fig. 8A and B), the spatial patterns in the SWE map (Fig. 8C) generally reflect the overall spatial pattern in snow depth. As discussed above (Fig. 1), the incorporation of spatial fields of snow density adds modest additional spatial complexity to the highly variable snow depth field. The coincident broadband albedo field (Fig. 8D) shows highest albedos in the higher elevations but with sensitivities to aspect, and decreasing albedo with decreasing elevation. These coincident mappings of SWE and albedo provide the first constraints for hydrologic modeling that can allow quantitative understanding of timing and magnitude of snowmelt runoff.

6.2. Post-processing

The ASO system provides a wide range of products with varying complexity to support water science and water applications. This includes fully distributed 3 m spatial resolution snow depth products all

the way to complete integration of basin snow water volume. These products were developed in consultation with partner water managers and are provided within 24 h of the ASO acquisition.

There are three main distillations of the ASO products that are distributed to current stakeholder partners: (i) fully distributed products and maps, (ii) semi-integrated products and maps as averaged per hydrologic-response unit (or modeling unit), sub-basin, or elevation bands, and (iii) basin-integrated products that aggregate the spatial fields to the simplest form. Of the fully distributed products, we distribute snow albedo and snow depth at 3 m spatial resolution and snow albedo and SWE at 50 m spatial resolution. Ancillary products such as land surface classification maps (delineating soil, vegetation, snow and water body) and snow depth change between each acquisition are also routinely produced.

With ASO acquisitions before and after snowfall events, we can also perform the first available quantitative analyses of snowfall dynamics, for example investigating orographic and convective dynamics in the context of mesoscale weather modeling. Moreover, the snowfall products will allow assessment of spatial precipitation estimates such as produced by the Precipitation Regression on Independent Slopes Model (PRISM; (Daly et al., 1994; Daly et al., 2008) or extrapolated from in situ measurements.

6.3. Spatial integrations

With the complete coverage of entire basins, ASO allows quantification of time series of basin SWE (Fig. 11). Many of the product deliverables are basin-integrated products that are summarized in the form of a SWE report (Fig. 12), in a format modeled after current operational products produced by other agencies. The SWE report provides the overall summary of the snow-covered area, percentage of snow cover extent in the basin, and estimated snow water content (in both acre-feet and cubic meters) along with several other basin-integrated statistics. The snow-free gridded elevation data are then used to summarize the SWE estimates in a similar way to the SWE report but for pre-specified elevation bands (e.g. every 1000 ft elevation interval) or for the case of the Tuolumne basin, high, mid and low elevation bands that have been historically used in water management (Fig. 13). The suite of products available to water managers is tuned through consultation and can be readily modified to suit the needs of stakeholders in specific basins.

For the Tuolumne basin, the water managers also use the Precipitation Runoff Modeling System (PRMS) to forecast inflows into the reservoir (Leavesley and Stannard, 1995). The PRMS relies on hydrologic response units (HRU) to disaggregate the basin into areas of coherent hydrologic function. To facilitate direct incorporation of the ASO SWE products into the forecasting system, both the spatially distributed SWE and snow albedo estimates are zonally averaged for each of the 280 HRU's in the Tuolumne PRMS model. The HRU-integrated SWE

```
calculate basin water volume in snowpack
*^*^*^*^*^*^*^*^*^*^*^*^*^*^*^*^*^*^*^*^*^*^*^*^*^*^*^*^*^*
Tuolumne River Basin
Airborne Snow Observatory
Date: 04/07/2014
surveyed area:                                  1175.5
snow covered area (km^2):                       1050.5
percent snow coverage :                           89.4
volume of snowpack water (m^3):          2.71301e+008
volume of snowpack water (acre-ft):             219947.
--  --  --  --  --  --  --  --  --  --  --  --
mean swe (m):                                     0.26
mean depth (m):                                   0.94
max depth (m):                                    6.33
min rho  (kg/m^3):                                64.2
max rho  (kg/m^3):                               545.7
mean rho (kg/m^3):                               294.0
*^*^*^*^*^*^*^*^*^*^*^*^*^*^*^*^*^*^*^*^*^*^*^*^*^*^*^*^*^*
```

Fig. 12. ASO report on integration of basin SWE from 50 m SWE distribution data for Tuolumne River Basin, April 7, 2014.

information is provided to the water managers as both a map (Fig. 14) and a data table for each metric. PRMS modeling with assimilated ASO data will be presented in subsequent manuscripts.

7. Validation

Here we present limited validation results for the principal ASO products, spectral albedo, snow depth, and SWE. Subsequent manuscripts currently in preparation will cover the broader set of validation activities.

The snow depth estimates generally have mean absolute errors of <8 cm, with bias <1 cm when compared with manually measured depths at the 15 × 15 m scale (Fig. 15). When coarsened from 3 m spatial resolution to 50 m, the error is reduced by $1/\sqrt{16.7}$ to <2 cm. These accuracies exceed the laser system specifications, and are as good or better than those reported elsewhere in the literature. While field validation surveys in steep and forested terrain have yet to be analyzed, the twin laser instrument and the 50% swath overlap provided by the CASI-constrained flight plan provide redundant measurements and multiple incidence angles within individual grid cells, and therefore should maintain normal error distributions from GPS-INS-induced horizontal and vertical errors and impart little bias when aggregated to the gridded data sets. Still, field validation and geometric analyses for complex terrain are needed going forward to have a more comprehensive understanding of the ASO snow depth uncertainties.

Snow density estimates from the model are compared throughout the season with all available snow course, in situ, and ASO field campaign measurements to confirm coherence between the model and

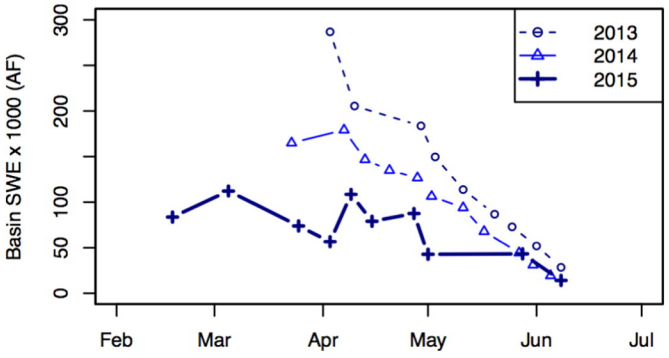

Fig. 11. Time series of the 2013–2015 basin-integrated snow water equivalent in the Tuolumne River Basin, in units of acre-ft, used by water managers.

```
Date: Wed Jun 10 07:29:15 2015
Flight: USCATB20150608f1a1
Exported by swe_at_3_elev_bands.pro
Band 1 =       1158.5 to      2073.1 m
Band 2 =       2073.1 to      2987.8 m
Band 3 =       2987.8 to      9000.0 m

Band          SWE Volume (AF)
SWE Band1              7.3
SWE Band2            994.3
SWE Band3          13300.6
```

Fig. 13. ASO report on distribution of SWE by elevation band that are distributed to water managers.

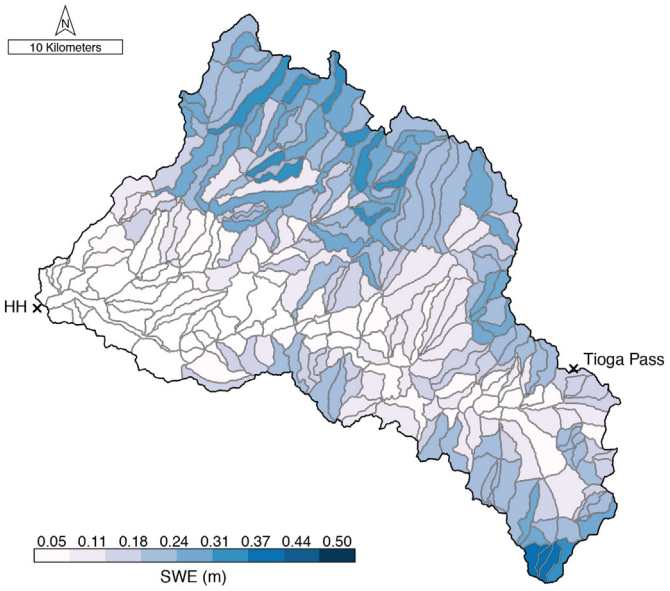

Fig. 14. PRMS hydrologic response unit (HRU) representation of ASO snow water equivalent for April 7, 2014.

the observations for each acquisition. The snow density fields from iSnobal for all three years of ASO operation are currently being evaluated in detail including propagation of uncertainty to basin SWE volumes. However, preliminary results based on in-situ pit and Federal Sampler measurements confirm that the modeled density errors are relatively small - on the order of 12–30 kg m^{-3} (3–8%) (Fig. 16). The data presented in Fig. 16 is derived from 180 sampling locations (shown in Fig. 9b), which range in elevation from 1980 to 3200 m, comprise of both exposed and vegetated site types (45 and 55% respectively) and reflect a range of solar exposure conditions. These snow density measurements were obtained during four field campaigns in the spring of 2013. From this breadth of data, the modeled density errors are within the expected measurement uncertainty (estimated at 11%, Conger and McClung, 2009) as well as the discrepancy of scale that is inherent when comparing point measurements to spatial fields.

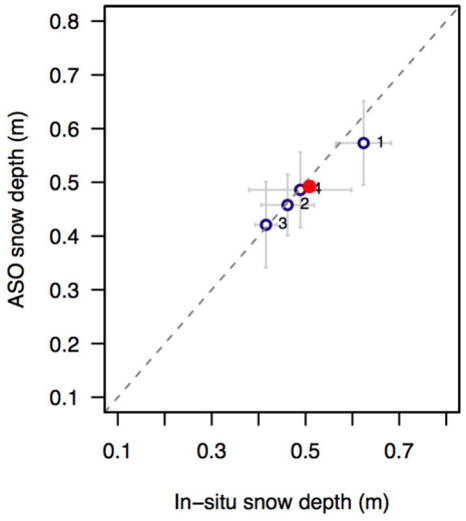

Fig. 15. Snow depth validation over a relatively flat but densely sampled area near Tioga Pass (n = 80 in-situ measurements). Each blue marker represents mean snow depths over a 15 × 15 m area, the red marker is the overall mean snow depth (with an overall bias of < 1 cm) and the grey bars show one standard deviation of the distribution. Refer to Fig. 14 for the location of Tioga Pass. (For interpretation of the references to color in this figure legend, the reader is referred to the web version of this article.)

Based on these preliminary snow density evaluation results, ASO operation typically applies two post-processing steps to the spatially distributed snow densities from iSnobal prior to conversion of snow depth to SWE. First, the modeled snow densities are corrected for an observed elevation bias, as shown by the linear error structure in Fig. 16a. The correction typically increases snow densities at high elevations (>2600 m) and reduces snow densities at lower elevations. Second, the bias-adjusted snow densities are further shifted in the *z*-direction to better suit in-situ observations. For example, if the mean snow density from the in-situ measurements is 400 kg m^{-3} and the mean modeled snow density at collocated pixels is 480 kg m^{-3} then the *z*-adjustment will act to reduce the modeled snow densities by a static value of ~80 kg m^{-3}. Generally the z-adjustment is much lower than 100 kg m^{-3} or <12%. Detailed impacts of these adjustments on basin-wide SWE will be addressed in future publications.

The uncertainties in SWE come from the combined uncertainties in snow depth and snow density. Our best understanding thus far is that snow depth uncertainty at the 3 m resolution is unbiased with RMSE of 0.08 m, resulting in depth uncertainty of <0.02 m at 50 m resolution. With the snow density uncertainties of 13–30 kg m^{-3} described above, we can estimate scenarios of SWE uncertainty. For a snowpack of 0.5 m depth and 100 kg m^{-3}, the SWE uncertainty is about 1 cm relative to the 5 cm actual. For a snowpack of 4.5 m depth and 450 kg m^{-3}, the SWE uncertainty is 10 cm relative to the 203 cm actual. Without bias, the integration of SWE to basin scale at 1100 km^2 would have uncertainty at markedly <1 mm or 1.1 M m^3 (<1000 acre-ft). Validation of and improvements in snow density modeling will be important in realizing such accuracies and providing comprehensive error estimates for ASO data products.

8. Conclusions

Though great strides have been made in our understanding of snow physical properties, snow hydrology, and glaciology, our ability to quantify the spatial distributions of snow mass and snow properties has, until now, been relatively simplistic, relying on assumed lapse rates, relationships with terrain variables, and sparse observations. Accordingly, operational estimates and forecasts of runoff and water availability have necessarily relied on indexed relationships that are calibrated to observations from prior years. These methods are vulnerable to unusual conditions – conditions not represented well in the period of record – in an increasingly variable hydroclimate and in a water resource environment that is subject to increasing demands and tightening supplies. New quantitative snow measuring capabilities are of critical importance.

While ASO data are currently available through the website at the Jet Propulsion Laboratory (aso.jpl.nasa.gov), more extensive archival and distribution is coming. As of writing, the ASO team is working with the National Snow and Ice Data Center Distributed Active Archive Center (NSIDC-DAAC) at the University of Colorado, Boulder to establish the hosting and archival of ASO data there. This partnership will allow more robust archival and user services to the global community, particularly as the program grows.

The Airborne Snow Observatory is taking important steps toward meeting these scientific and operational needs. By making relatively straightforward and direct measurement of snow depth at high resolution, ASO captures the primary source of spatial variability in snow mass in mountain watersheds, and by integration with snow density observations and modeling, the first basin-wide, repeat estimates of SWE have been made available. ASO also quantifies the primary snow property determinant of snowmelt rate, the snow albedo. The ASO computing infrastructure importantly provides the capacity to deliver high quality data products to water management partners on operationally relevant time scales of <24 h. Together, the ASO approach provides a pathway to advance hydrologic science in snow-dominated regions, and to enable the next generation of resilient and adaptive water management.

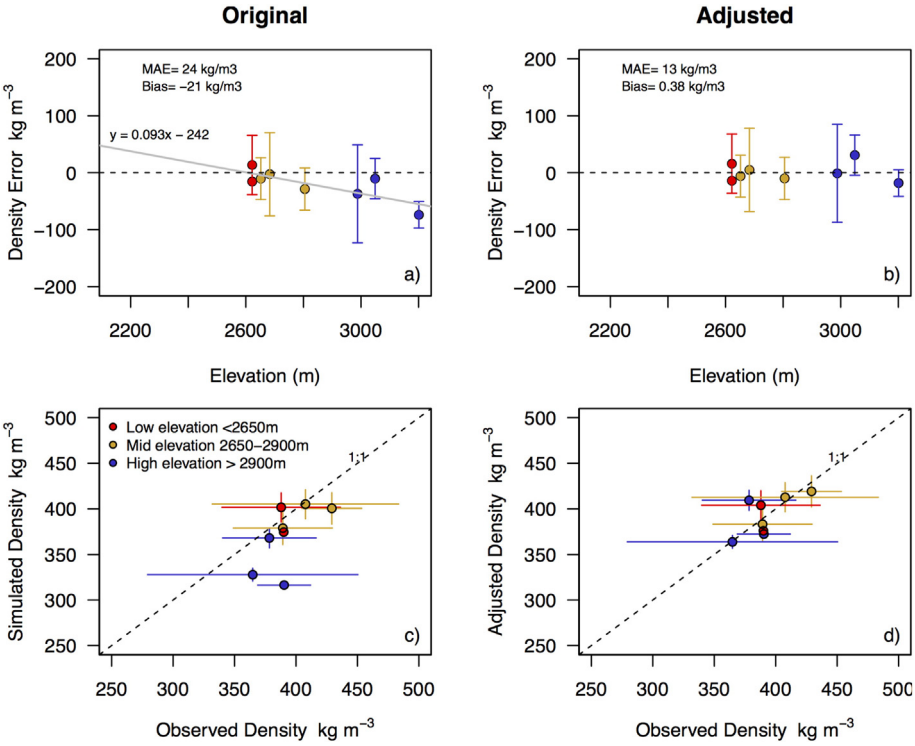

Fig. 16. Validation and demonstration of snow density post-processing with (A) modeled snow density errors and linear elevation-dependent error structure, (B) bias-corrected snow density errors, (C) modeled snow density dynamic range colored by elevation band and (D) bias-corrected snow density dynamic range. These data were derived from a comparison with n = 180 in-situ measurements (Fig. 8).

Acknowledgments

Funding for the Airborne Snow Observatory was provided by NASA, the California Department of Water Resources, JPL investments, Colorado Water Conservation Board, City of San Francisco Public Utilities Commission, Turlock Irrigation District, and Modesto Irrigation District, and USDA Agricultural Research Service. Modeling and density simulations were conducted at the Northwest Watershed Research Center in Boise, Idaho. Part of this work was performed at the Jet Propulsion Laboratory, California Institute of Technology under a contract with NASA.

References

Asner, G.P., Knapp, D.E., Boardman, J., Green, R.O., Kennedy-Bowdoin, T., Eastwood, M., Martin, R.E., Anderson, C., Field, C.B., 2012. Carnegie airborne observatory-2: increasing science data dimensionality via high-fidelity multi-sensor fusion. Remote Sens. Environ. 124, 454–465. http://dx.doi.org/10.1016/j.rse.2012.06.012.

Asner, G.P., Mascaro, J., Anderson, C., Knapp, D.E., Martin, R.E., Kennedy-Bowdoin, T., Breugel, M.v., Davies, S., Hall, J.S., Muller-Landau, H.C., Potvin, C., Sousa, W., Wright, J., Bermingham, E., 2013. High-fidelity national carbon mapping for resource management and REDD+. Carbon Balance Manage. 8 (7), 1–14. http://dx.doi.org/10.1186/1750-0680-8-7.

Bales, R.C., Molotch, N.P., Painter, T.H., Dettinger, M.D., Rice, R., Dozier, J., 2006. Mountain hydrology of the western United States. Water Resour. Res. 42, W08432. http://dx.doi.org/10.1029/2005WR004387.

Bamber, J., Rivera, A., 2007. A review of remote sensing methods for glacier mass balance determination. Glob. Planet. Chang. 59, 138–148 (doi: :10.1016/j.gloplacha.2006.11.031).

Barnett, T.P., Adam, J.C., Lettenmaier, D.P., 2005. Potential impacts of a warming climate on water availability in snow-dominated regions. Nature 438. http://dx.doi.org/10.1038/nature04141.

Bartelt, P., Lehning, M., 2002. A physical SNOWPACK model for the Swiss avalanche warning. Cold Reg. Sci. Technol. 35 (3), 123–145. http://dx.doi.org/10.1016/S0165-232X(02)00074-5.

Blöschl, G., 1991. The influence of uncertainty in air temperature and albedo on snowmelt. Nord. Hydrol. 22, 95–108.

Bormann, K.J., Westra, S., Evans, J.P., McCabe, M.F., 2013. Spatial and temporal variability in seasonal snow density. J. Hydrol. 484, 63–73. http://dx.doi.org/10.1016/j.jhydrol.2013.01.032.

Bryant, A.C., Painter, T.H., Deems, J.S., Bender, S.M., 2013. Impact of dust radiative forcing in snow on accuracy of operational runoff prediction in the upper Colorado River Basin. Geophys. Res. Lett. http://dx.doi.org/10.1002/grl.50773 (in press).

Carroll, T., 2001. Airborne Gamma Radiation Snow Survey Program. National Operational Hydrologic Remote Sensing Center, Chanhassen Minnesota (1-14 pp).

Chang, A.T.C., Foster, J.L., Hall, D.K., 1996. Effects of forest on the snow parameters derived from microwave measurements during the BOREAS winter field campaign. Hydrol. Process. 10, 1565–1574.

Christensen, N.S., Lettenmaier, D.P., 2007. A multimodel ensemble approach to assessment of climate change impacts on the hydrology and water resources of the Colorado River Basin. Hydrol. Earth Syst. Sci. 11, 1417–1434. http://dx.doi.org/10.5194/hess-11-1417-2007.

Christensen, N.S., Wood, A.W., Lettenmaier, D.P., Palmer, R.N., 2004. Effects of climate change on the hydrology and water resources of the Colorado River Basin. J. Hydroclimatol. 62, 337–363.

Clow, D., 2010. Changes in the timing of snowmelt and streamflow in Colorado: a response to recent warming. J. Clim. 23 (9), 2293–2306. http://dx.doi.org/10.1175/2009JCLI2951.1.

Conger, S.M., McClung, D.M., 2009. Comparison of density cutters for snow profile observations. J. Glaciol. 55, 163–169. http://dx.doi.org/10.3189/002214309788609038.

Daly, C., Neilson, R.P., Phillips, D.L., 1994. A statistical-topographic model for mapping climatological precipitation over mountainous terrain. J. Appl. Meteorol. 33, 140–158.

Daly, C., Halbleib, M., Smith, J.I., Gibson, W.P., Doggett, M.K., Taylor, G.H., Curtis, J., Pasteris, P.A., 2008. Physiographically-sensitive mapping of temperature and precipitation across the conterminous United States. Int. J. Climatol. 28, 2031–2064. http://dx.doi.org/10.1002/joc.1688.

Deems, J.S., Fassnacht, S.R., Elder, K.J., 2006. Fractal distribution of snow depth from LiDAR data. J. Hydrometeorol. 7 (2), 285–297. http://dx.doi.org/10.1175/JHM487.1.

Deems, J.S., Painter, T.H., Finnegan, D.C., 2013a. Lidar measurement of snow depth: a review. J. Glaciol. 59 (215), 467–479. http://dx.doi.org/10.3189/2013JoG12J154.

Deems, J.S., Painter, T.H., Barsugli, J.J., Belnap, J., Udall, B., 2013b. Combined impacts of current and future dust deposition and regional warming on Colorado River Basin snow dynamics and hydrology. Hydrol. Earth Syst. Sci. 10, 6237–6275. http://dx.doi.org/10.5194/hessd-10-6237-2013.

Deems, J.S., Gadomski, P.J., Vellone, D., Evanczyk, R., LeWinter, A.L., Birkeland, K.W., Finnegan, D.C., 2015. Mapping starting zone snow depth with a ground-based lidar to assist avalanche control and forecasting. Cold Reg. Sci. Technol. 120, 197–204.

Dozier, J., 2011. Mountain hydrology, snow color, and the fourth paradigm. EOS Trans. Am. Geophys. Union 92, 373–375. http://dx.doi.org/10.1029/2011EO430001.

Dozier, J., Schneider, S.R., McGinnis Jr., D.F., 1981. Effect of grain size and snowpack water equivalence on visible and near-infrared satellite observations of snow. Water Resour. Res. 17 (4), 1213–1221.

Dozier, J., Green, R.O., Nolin, A.W., Painter, T.H., 2009. Interpretation of snow properties from imaging spectrometry. Remote Sens. Environ. 113, 525–537. http://dx.doi.org/10.1016/j.rse.2007.07.029.

Evans, J.S., Hudak, A.T., 2007. A multiscale curvature algorithm for classifying discrete return LiDAR in forested environments. Geosci. Remote Sens. 45 (4), 1029–1038. http://dx.doi.org/10.1109/TGRS.2006.890412.

Flerchinger, G.N., Cooley, K.R., Deng, Y., 1994. Impacts of spatially and temporally varying snowmelt on subsurface flow in a mountainous watershed: 1. Snowmelt simulation. Hydrol. Sci. 39, 507–519.

Garen, D.C., Marks, D., 2005. Spatially distributed energy balance snowmelt modelling in a mountainous river basin: estimation of inputs and verification of model results. J. Hydrol. 315 (1–4), 126–153. http://dx.doi.org/10.1016/j.jhydrol.2005.03.026.

Green, R.O., Eastwood, M.L., Sarture, C.M., Chrien, T.G., Aronsson, M., Chippendale, B.J., Faust, J.A., Pavri, B.E., Chovit, C.J., Solis, M., Olah, M.R., Williams, O., 1998. Imaging spectroscopy and the airborne visible/infrared imaging spectrometer. Remote Sens. Environ. 65, 227–248.

Green, R.O., Painter, T.H., Roberts, D.A., Dozier, J., 2006. Measuring the three phases of water in a melting snow environment with an imaging spectrometer in the solar reflected spectrum. Water Resour. Res. http://dx.doi.org/10.1029/2005WR004509.

Hamlet, A.F., Mote, P.W., Clark, M.P., Lettenmaier, D.P., 2005. Effects of temperature and precipitation variability on snowpack trends in the western United States. J. Clim. 18 (21), 4545–4561.

Hamlet, A.F., Mote, P.W., Clark, M.P., Lettenmaier, D.P., 2007. Twentieth-century trends in runoff, evapotranspiration, and soil moisture in the western United States. J. Clim. 20, 1468–1486. http://dx.doi.org/10.1175/JCLI4051.1.

Hopkinson, C., Sitar, M., Chasmer, L., Treitz, P., 2004. Mapping snowpack depth beneath forest canopies using airborne lidar. Photogramm. Eng. Remote. Sens. 70, 323–330. http://dx.doi.org/10.14358/PERS.70.3.323.

Jonas, T., Marty, C., Magnusson, I., 2009. Estimating the snow water equivalent from snow depth measurements in the Swiss Alps. J. Hydrol. 378, 161–167. http://dx.doi.org/10.1016/j.jhydrol.2009.09.021.

Jordan, R., 1991. A One-dimensional Temperature Model for a Snow Cover Special Report 91–6. US Army Cold Regions Research and Engineering Laboratory, Hanover, NH.

Kampe, T.U., Johnson, B.R., Kuester, M., Keller, M., 2010. NEON: the first continental-scale ecological observatory with airborne remote sensing of vegetation canopy biochemistry and structure. J. Appl. Remote. Sens. 4 (043510). http://dx.doi.org/10.1117/1.3361375.

Kirnbauer, R., Blöschl, G., Gutknecht, D., 1994. Entering the era of distributed snow models. Nord. Hydrol. 25 (1–2), 1–24.

Kormos, P., Marks, D., McNamara, J., Marshall, H.P., Winstral, A., Flores, A., 2014. Snow distribution, melt and surface water inputs to the soil in the mountain rain-snow transition zone. J. Hydrol. 519 (Part A), 190–204. http://dx.doi.org/10.1016/j.jhydrol.2014.06.051.

Kumar, M., Marks, D., Dozier, J., Reba, M., Winstral, A., 2013. Evaluation of distributed hydrologic impacts of temperature-index and energy-based snow model simulations. Adv. Water Resour. 56, 77–89. http://dx.doi.org/10.1016/j.advwatres.2013.03.006.

Leavesley, G.H., Stannard, L.G., 1995. The precipitation-runoff modeling system - PRMS. In: Singh, V.P. (Ed.), Computer Models of Watershed Hydrology, pp. 281–310.

Link, T., Marks, D., 1999. Distributed simulation of snowcover mass and energy balance in a boreal forest. Hydrol. Process. 13 (13–14), 2439–2452. http://dx.doi.org/10.1002/(SICI)1099-1085(199910)13:14/15<2439::AID-HYP866>3.0.CO;2-1.

Luojus, K., Pulliainen, J., Takala, M., Lemmetyinen, J., Kangwa, M., Smolander, T., Derksen, C., 2013. Global snow monitoring for climate research - GlobSnow algorithm theoretical basis document - SWE-algorithm. Eur. Space Agency (35 pp).

Marks, D., Dozier, J., 1992. Climate and energy exchange at the snow surface in the alpine region of the Sierra Nevada. 2. Snow cover energy balance. Water Resour. Res. 28 (11), 3043–3054.

Marks, D., Winstral, A., Seyfried, M., 2002. Simulation of terrain and forest shelter effects on patterns of snow deposition, snowmelt and runoff over a semi-arid mountain catchment. Hydrol. Process. 16 (18), 3605–3626. http://dx.doi.org/10.1002/hyp.1237.

Mattmann, C., 2009. A reusable process control system framework for the orbiting carbon observatory and NPP Sounder PEATE missions. 3rd IEEE International Conference on Space Mission Challenges for Information Technology, IEEE, pp. 165–172.

Mattmann, C., Crichton, D., Medvidovic, N., Hughes, J.S., 2006. A Software Architecture-based Framework for Highly Distributed and Data-intensive Applications. Software Engineering Achievements Track, Shanghai, China, ICSE, pp. 721–730.

Mattmann, C., Zitting, J., 2011. Tika in action. Manning Publications, Greenwich, CT, USA.

Mie, G., 1908. Beiträge zur Optik trüber Medien, Speziell Kolloidaler Metallösungen. Ann. Phys. 25, 377–445.

Mote, P.W., Hamlet, A.F., Clark, M.P., Lettenmaier, D.P., 2005. Declining mountain snowpack in western North America. Bull. Am. Meteorol. Soc. 86 (1), 39–49. http://dx.doi.org/10.1175/BAMS-86-1-39.

Mott, R., Schirmer, M., Lehning, M., 2011. Scaling properties of wind and snow depth distribution in an Alpine catchment. J. Geophys. Res. - Atmos. 116. http://dx.doi.org/10.1029/2010JD014886.

Munson, S.M., Belnap, J., Okin, G.S., 2011. Responses of wind erosion to climate-induced vegetation changes on the Colorado Plateau. Proc. Natl. Acad. Sci. 108 (10), 3854–3859. http://dx.doi.org/10.1073/pnas.1014947108.

Nayak, A., Marks, D., Chandler, D., Winstral, A., 2012. Modeling inter-annual variability in snowcover development and melt at a semi-arid mountain catchment. J. Hydrol. Eng. 17, 74–85. http://dx.doi.org/10.1061/(ASCE)HE.1943-5584.0000408.

Nolin, A.W., Daly, C., 2006. Mapping "at risk" snow in the Pacific Northwest. J. Hydrometeorol. 7, 1164–1171. http://dx.doi.org/10.1175/JHM543.1.

Nolin, A.W., Dozier, J., 2000. A hyperspectral method for remotely sensing the grain size of snow. Remote Sens. Environ. 74 (2), 207–216.

Oerlemans, J., 2000. Analysis of a 3 year meteorological record from the ablation zone of Morteratschgletscher, Switzerland: energy and mass balance. J. Glaciol. 46 (155), 571–579. http://dx.doi.org/10.3189/172756500781832657.

Painter, T.H., Dozier, J., 2004a. The effect of anisotropic reflectance on imaging spectroscopy of snow parameters. Remote Sens. Environ. 89 (4), 409–422.

Painter, T.H., Dozier, J., 2004b. Measurements of the hemispherical-directional reflectance of snow at fine spectral and angular resolution. J. Geophys. Res.-Atmos. 109, D18115. http://dx.doi.org/10.1029/2003JD004458.

Painter, T.H., Roberts, D.A., Green, R.O., Dozier, J., 1998. The effect of grain size on spectral mixture analysis of snow-covered area from AVIRIS data. Remote Sens. Environ. 65 (3), 320–332.

Painter, T.H., Duval, B., Thomas, W.H., Mendez, M., Heintzelman, S., Dozier, J., 2001. Detection and quantification of snow algae with an airborne imaging spectrometer. Appl. Environ. Microbiol. 67 (11), 5267–5272. http://dx.doi.org/10.1128/AEM.67.11.5267–5272.2001.

Painter, T.H., Dozier, J., Roberts, D.A., Davis, R.E., Green, R.O., 2003. Retrieval of subpixel snow-covered area and grain size from imaging spectrometer data. Remote Sens. Environ. 85 (1), 64–77. http://dx.doi.org/10.1016/S0034-4257(02)00187-6.

Painter, T.H., Barrett, A.P., Landry, C.C., Neff, J.C., Cassidy, M.P., Lawrence, C.R., McBride, K.E., Farmer, G.L., 2007. Impact of disturbed desert soils on duration of mountain snow cover. Geophys. Res. Lett. 34, L12502. http://dx.doi.org/10.1029/2007GL030284.

Painter, T.H., Deems, J.S., Belnap, J., Hamlet, A.F., Landry, C.C., Udall, B., 2010. Response of Colorado River runoff to dust radiative forcing in snow. Proc. Natl. Acad. Sci. 107 (40), 17125–17130. http://dx.doi.org/10.1073/pnas.0913139107.

Painter, T.H., Skiles, S.M., Deems, J.S., Bryant, A.C., Landry, C.C., 2012. Dust radiative forcing in snow of the Upper Colorado River Basin: part I. A 6 year record of energy balance, radiation, and dust concentrations. Water Resour. Res. 48 (7), 1–14. http://dx.doi.org/10.1029/2012WR011985.

Painter, T.H., Seidel, F., Bryant, A.C., Skiles, S.M., Rittger, K., 2013. Imaging spectroscopy of albedo and radiative forcing by light absorbing impurities in mountain snow. J. Geophys. Res. - Atmos. 118 (17), 9511–9523. http://dx.doi.org/10.1029/2012JD019398.

Painter, T.H., Skiles, S.M., Deems, J.S., 2015. Interannual variation of snowmelt runoff hydrographs in the Eastern Colorado River Basin controlled by dust radiative forcing. Proc. Natl. Acad. Sci. U. S. A. (in review).

Peck, E., Carroll, T., Vandermark, S., 1980. Operational aerial snow surveying in the United States. Hydrol. Sci. Bull. 25, 51–62.

Prokop, A., 2008. Assessing the applicability of terrestrial laser scanning for spatial snow depth measurements. Cold Reg. Sci. Technol. 54, 155–163. http://dx.doi.org/10.1016/j.coldregions.2008.07.002.

Rasouli, K., Pomeroy, J., Marks, D., 2015. Snowpack sensitivity to perturbed climate changes in alpine catchments. Hydrol. Process. http://dx.doi.org/10.1002/hyp.10587.

Reba, M., Marks, D., Winstral, A., Link, T., Kumar, M., 2011. Sensitivity of the snowcover in a mountain basin to variations in climate. Hydrol. Process. 25 (21), 3312–3321. http://dx.doi.org/10.1002/hyp.8155.

Richter, R., Schläpfer, D., 2011. Atmospheric/Topographic Correction for Airborne Imagery. DLR, Wessling, Germany (194 pp).

Rieger, P., Ullrich, A., 2011. Resolving range ambiguities in high-repetition rate airborne lidar applications. Proc. IEEE 8186. http://dx.doi.org/10.1117/12.898551 (81860A–81860A-8).

Schaepman-Strub, G., Schaepman, M., Painter, T.H., Dangel, S., Martonchik, J.V., 2006. Reflectance quantities in optical remote sensing - definitions and case studies. Remote Sens. Environ. 103 (1), 27–42.

Shi, J.C., Dozier, J., 2000a. Estimation of snow water equivalence using SIR-C/X-SAR, part I: inferring snow density and subsurface properties. IEEE Trans. Geosci. Remote Sens. 38 (6), 2465–2474.

Shi, J.C., Dozier, J., 2000b. Estimation of snow water equivalence using SIR-C/X-SAR, part II: inferring snow depth and grain size. IEEE Trans. Geosci. Remote Sens. 38 (6), 2475–2488.

Skiles, S.M., Painter, T.H., Deems, J.S., Bryant, A.C., Landry, C.C., 2012. Dust radiative forcing in snow of the Upper Colorado River Basin: part II. Interannual variability in radiative forcing and snowmelt rates. Water Resour. Res. 48 (7), 11. http://dx.doi.org/10.1029/2012WR011986.

Sorman, A.U., Akyurek, Z., Sensoy, A., Sorman, A.A., Tekeli, A.E., 2007. Commentary on comparison of MODIS snow cover and albedo products with ground observations over the mountainous terrain of Turkey. Hydrol. Earth Syst. Sci. 11, 1353–1360.

Sproles, E., Nolin, A.W., Rittger, K., Painter, T.H., 2013. Climate change impacts on maritime mountain snowpack in the Oregon Cascades. Hydrol. Earth Syst. Sci. 9, 13037–13081. http://dx.doi.org/10.5194/hessd-9-13037-2012.

Stamnes, K., Tsay, S.-C., Wiscombe, W.J., Jayaweera, K., 1988. Numerically stable algorithm for discrete-ordinate-method radiative transfer in multiple scattering and emitting layered media. Appl. Opt. 27, 2502–2509.

Stroeve, J., Box, J., Gao, F., Liang, S., Nolin, A., Schaaf, C.B., 2005. Accuracy assessment of the MODIS 16-albedo product for snow: comparison with Greenland in situ measurements. Remote Sens. Environ. 94 (1), 46–60.

Sturm, M., Holmgren, J., 1998. Differences in compaction behavior of three climate classes of snow. Ann. Glaciol. 26, 125–130.

Sturm, M., Taras, B., Liston, G.E., Derksen, C., Jonas, T., Lea, J., 2010. Estimating snow water equivalent using snow depth data and climate classes. J. Hydrometeorol. 11, 1380–1394. http://dx.doi.org/10.1175/2010JHM1202.1.

Takala, M., Luojus, K., Pulliainen, J., Derksen, C., Lemmetyinen, J., Kärnä, J.-P., Koskinen, J., 2011. Estimating northern hemisphere snow water equivalent for climate research through assimilation of space-borne radiometer data and ground-based measurements. Remote Sens. Environ. 115, 3517–3529. http://dx.doi.org/10.1016/j.rse.2011.08.014.

Tarboten, D.G., Luce, C.H., 1996. Utah Energy Balance Snow Accumulation and Melt Model (UEB) Computer Model Technical Description and Users Guide. Utah Water Research Laboratory and USDA Forest Service Intermountain Research Station (64 pp).

Tarboton, D.G., Jackson, T.H., Liu, J.Z., Neale, C.M.U., Cooley, K.R., McDonnell, J.J., 1995. A Grid Based Distributed Hydrologic Model: Testing Against Data From Reynolds Creek Experimental Watershed. American Meteorological Society Conference on Hydrology, Dallas, Texas.

Trujillo, E., Ramirez, J.A., Elder, K.J., 2007. Topographic, meteorologic, and canopy controls on the scaling characteristics of the spatial distribution of snow depth fields. Water Resour. Res. 43.

Wagner, W., Ullrich, A., Ducic, V., Melzer, T., Studnicka, N., 2006. Gaussian decomposition and calibration of a novel small-footprint full-waveform digitising airborne laser scanner. ISPRS J. Photogramm. Remote Sens. 60, 100–112. http://dx.doi.org/10.1016/j.isprsjprs.2005.12.001.

Wang, Z., Schaaf, C.B., Chopping, M.J., Strahler, A.H., Wang, J., Roman, M.O., Rocha, A.V., Woodcock, C.E., Shuai, Y., 2012. Evaluation of moderate-resolution imaging spectroradiometer (MODIS) snow albedo product (MCD43A) over tundra. Remote Sens. Environ. 117, 264–280.

Yueh, S.H., Dinardo, S.J., Akgiray, A., West, R., Cline, D.W., Elder, K., 2009. Airborne Ku-band polarimetric radar remote sensing of terrestrial snow cover. IEEE Trans. Geosci. Remote Sens. 47 (10), 3347–3364. http://dx.doi.org/10.1109/TGRS.2009.2022945.